Chaos, Solitons and Fractals 153 (2021) 111488

Contents lists available at ScienceDirect

Chaos, Solitons and Fractals

Nonlinear Science, and Nonequilibrium and Complex Phenomena

journal homepage: www.elsevier.com/locate/chaos

Frontiers

Chaos on a saturable optical dimer

Rodrigo A. Vicencio*, Marcel G. Clerc

Departamento de Física and Millenium Institute for Research in Optics - MIRO, Facultad de Ciencias Físicas y Matemáticas, Universidad de Chile, Chile

ARTICLE INFO

Article history:
Received 2 September 2021
Accepted 25 September 2021

Keywords:
Chaos
Waveguides
Dimers

ABSTRACT

A pair of periodically coupled and forced simple oscillators can exhibit aperiodic behaviors. Here we study the effect of periodic spatial modulations in an optical dimer composed of photorefractive saturable waveguides. The propagation of light along these waveguides as a function of the initial condition exhibits chaotic behaviors. The dynamical behaviors are elucidated based on the adequate representation of the variables, frequency spectra, and Poincaré sections. Homoclinic and heteroclinic entanglements associated with the hyperbolic points that separate the stable equilibria are the origin of the chaotic behavior. The different dynamical regimes have been characterized as a function of light power and initial conditions. Our results open the possibility of using optical saturable dimers in the secure transmission of information.

1. Introduction

Oscillators and their dynamics have attracted the attention of physics from their dawn, being the pendulum, one of the first mechanical examples studied due to its potential application as a watch [1,2]. An oscillator is a system that is characterized by being able to exhibit a periodic or quasi-periodic evolution around an equilibrium. The most common examples come from classical mechanics (pendulum and spring mass system), electricity (electrical circuits), and quantum mechanics (atoms and molecules), but the oscillators are observed in all the natural sciences ranging from biology, chemistry to physics. A single oscillator for small disturbances is characterized by exhibiting harmonic movement, which is one of the elementary behaviors of physics. When the disturbances are increased, nonlinear terms modify the harmonic oscillations but the oscillations persist [3]. This scenario changes radically when one couples two oscillators [4]. Small disturbances exhibit different normal modes, coherence oscillations [5]. However, the connection of the different attractive and repulsive manifolds of unstable (hyperbolic) equilibria produces chaotic behaviors [6–8]. Indeed, this heteroclinic entanglement produces exponential sensitivity around the hyperbolic points. This type of chaotic behavior is observed in conservative or non-conservative systems. In the case of two simple coupled oscillators in conservative systems, chaotic behaviors are not observed due to conserved quantities. The coupling of other oscillators or the inclusion of external forcing can induce chaotic behaviors [8–11]. A simple system of two coupled conservative oscillators in optics is a nonlinear coherent coupler—*optical dimers*—consisting of two coupled waveguides (see Fig. 1) [12,13]. A dimer formed by photorefractive saturable waveguides shows different equilibria with regular behaviors. Indeed, this system is integrable [13], that is, the solutions can be expressed in terms of integrals and the phase space can be characterized employing simple curves [14]. Namely, the phase space is of foliated nature. Integrable systems are structurally fragile, that is, under system modifications, integrability is lost and chaotic behavior emerges.

The paper aims to investigate the effect of periodic spatial modulations in an optical dimer composed of photorefractive saturable waveguides. These spatial modulations are responsible for the emergence of chaotic behaviors when light propagates along these waveguides as a function of the initial condition and light power. Adequate representation of the physical variables, frequency spectra, and Poincaré sections allow us to reveal the complex dynamic behaviors.

The article is organized as follows. The spatial unmodulated optical dimer model composed of saturable photorefractive waveguides and its analytical characterization of dynamical behaviors are presented in Section 2. Detailed characterization of the integrable optical dimer dynamics employing the frequency spectrum and phase space is presented in Section 3. In Section 4, the spatial modulation of the dimer is incorporated, generating chaotic behaviors. In addition, a detailed characterization of the frequency spectrum and Poincaré sections for different powers are presented. *Conclusions are presented in Section 4.*

* Corresponding author.
E-mail addresses: rvicencio@uchile.cl (R.A. Vicencio), marcel@dfi.uchile.cl (M.G. Clerc).

https://doi.org/10.1016/j.chaos.2021.111488
0960-0779/

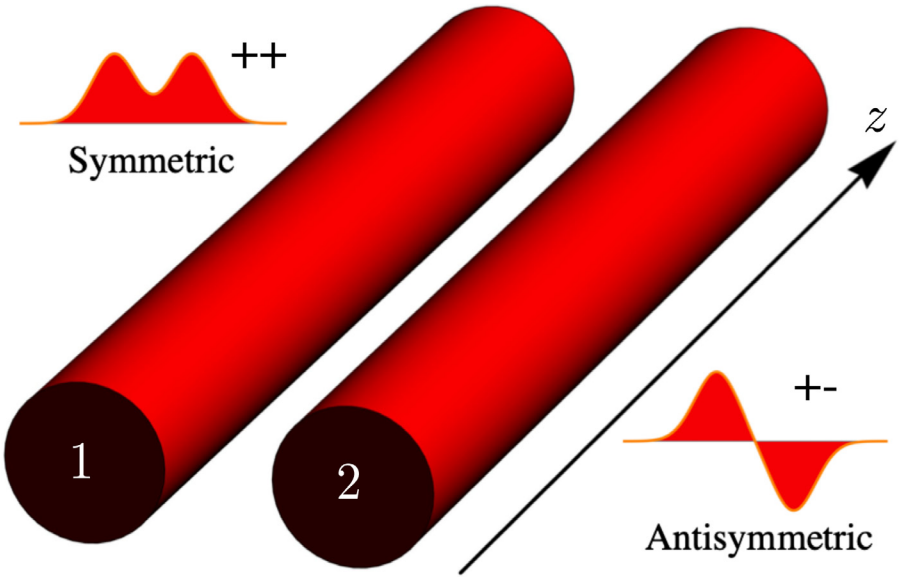

Fig. 1. Schematic representation of a saturable dimer, which is composed of two waveguides (represented by the red cylinders) separated by a given distance. z accounts for the propagation direction along waveguides. Insets depict the symmetric and asymmetric mode profiles. (For interpretation of the references to colour in this figure legend, the reader is referred to the web version of this article.)

2. Model of the spatial unmodulated optical dimer

Light propagation on an array formed by single-mode identical nonlinear photorefractive saturable waveguides (as sketched in Fig. 1) is well described by a dimensionless saturable discrete nonlinear Schrödinger equation (s-DNLE) [13], which for two coupled waveguides reads as

$$\begin{aligned} -i\frac{\partial u_1}{\partial z} &= Vu_2 - \frac{\gamma u_1}{1+|u_1|^2} \\ -i\frac{\partial u_2}{\partial z} &= Vu_1 - \frac{\gamma u_2}{1+|u_2|^2}. \end{aligned} \tag{1}$$

Here, $u_n(z)$ corresponds to the fundamental mode complex amplitude at the n-th site ($n = 1$ and 2); $\gamma > 0$ accounts for a focusing nonlinearity; V defines the coupling coefficient between both waveguides, which decays exponentially with the distance between waveguides [16]. z is the dynamical variable in this model and stands for the propagation distance along waveguides. Model (1) possesses two conserved quantities, the Power

$$P(z) = P_1(z) + P_2(z) \equiv |u_1(z)|^2 + |u_2(z)|^2, \tag{2}$$

and the Hamiltonian

$$H \equiv -V(u_2u_1^* + u_2^*u_1) + \gamma \log\left[(1+|u_1|^2)(1+|u_2|^2)\right], \tag{3}$$

which are useful to study the dynamical properties as well as to check numerical accuracy. As the model (1) has two degrees of freedom and two conserved quantities is fully integrable [14,15]. Therefore, we can find stationary (steady state) solutions analytically, in the linear and nonlinear regimes, of the form $u_n(z) = U_n \exp[i\lambda z]$, where λ corresponds to the solution frequency and U_n amplitudes are real. It is simple to show that complex solutions only exist for two defined phases 0 or π, therefore, amplitudes can be simply treated as real quantities. As a consequence, model (1) reduces to two algebraic equations

$$\lambda U_1 = VU_2 - \frac{\gamma U_1}{1+U_1^2} \quad \lambda U_2 = VU_1 - \frac{\gamma U_2}{1+U_2^2}. \tag{4}$$

Notice that saturable models possess two linear regimes, at low and high powers [17–19]. When light power is low, term $1 + U_n^2 \approx 1$ and equations are completely linear with two eigenfrequencies given by $\lambda = \pm V - \gamma$, for symmetric (++) and antisymmetric (+−) modes, respectively. Mode profiles are sketched as insets in Fig. 1. On the other hand, when power is very high saturation term becomes negligible $[1/(1+U_n^2) \ll 1]$ and equations become linear again. In this high-power regime, eigenfrequencies simply become $\lambda = \pm V$ for ++ and +− modes, respectively. Both limits define the existence region for solutions on a P versus λ diagram [13,19].

For low power, model (1) transforms directly into a cubic dimer model [10], in which $-\gamma u_n/(1+|u_n|^2) \approx \gamma|u_n|^2u_n - \gamma u_n$. Therefore, the dynamical picture is very well-known, including chaos prediction [9–11,20,21]. In that case, for low power, there are only two (++ and +−) fundamental nonlinear stationary solutions, which become four at larger powers, with two degenerated and equivalent asymmetric states bifurcating at the ++ (+−) solution for positive (negative) nonlinearity. In that case, the asymmetric solution is always stable, while the symmetric or asymmetric solution loses stability and transforms into a hyperbolic point, been responsible of generating chaotic dynamics.

Nonlinear stationary solutions for coupled Eq. (4) are found using a standard method based on equilibrium states [13]. Considering the ansatz $U_1 = A$ and $U_2 = \alpha A$, where A and α are real constants. Inserting this ansatz in (4) and, after straightforward calculations, we obtain

$$\alpha = \pm 1 \quad \alpha_\pm = \frac{\gamma A^2 \pm \sqrt{\gamma^2A^4 - 4V^2(1+A^2)^2}}{2VA^2(1+A^2)}. \tag{5}$$

We find four stationary solutions, where two of them are trivial and have exactly the same form than the linear ones. Hence, these solutions bifurcate at the linear modes at low power ($\lambda = \pm V - \gamma$), while disappearing at high power ($\lambda = \pm V$). For $\gamma > 0$, the nontrivial solutions ($\alpha_\pm$) bifurcate from the symmetric solution ++ at two different power regions which depend on nonlinearity γ [13]. Although we can construct a P versus λ diagram for all these solutions, we focus on constructing an effective potential representation, which captures the main dynamical features of this model and gives us all the dynamically connected nonlinear stationary solutions as well. Using a reduced center of mass "$\bar{x}$" as a key dynamical parameter, we simply define as $\bar{x} \equiv P_2/P$. Note that the real

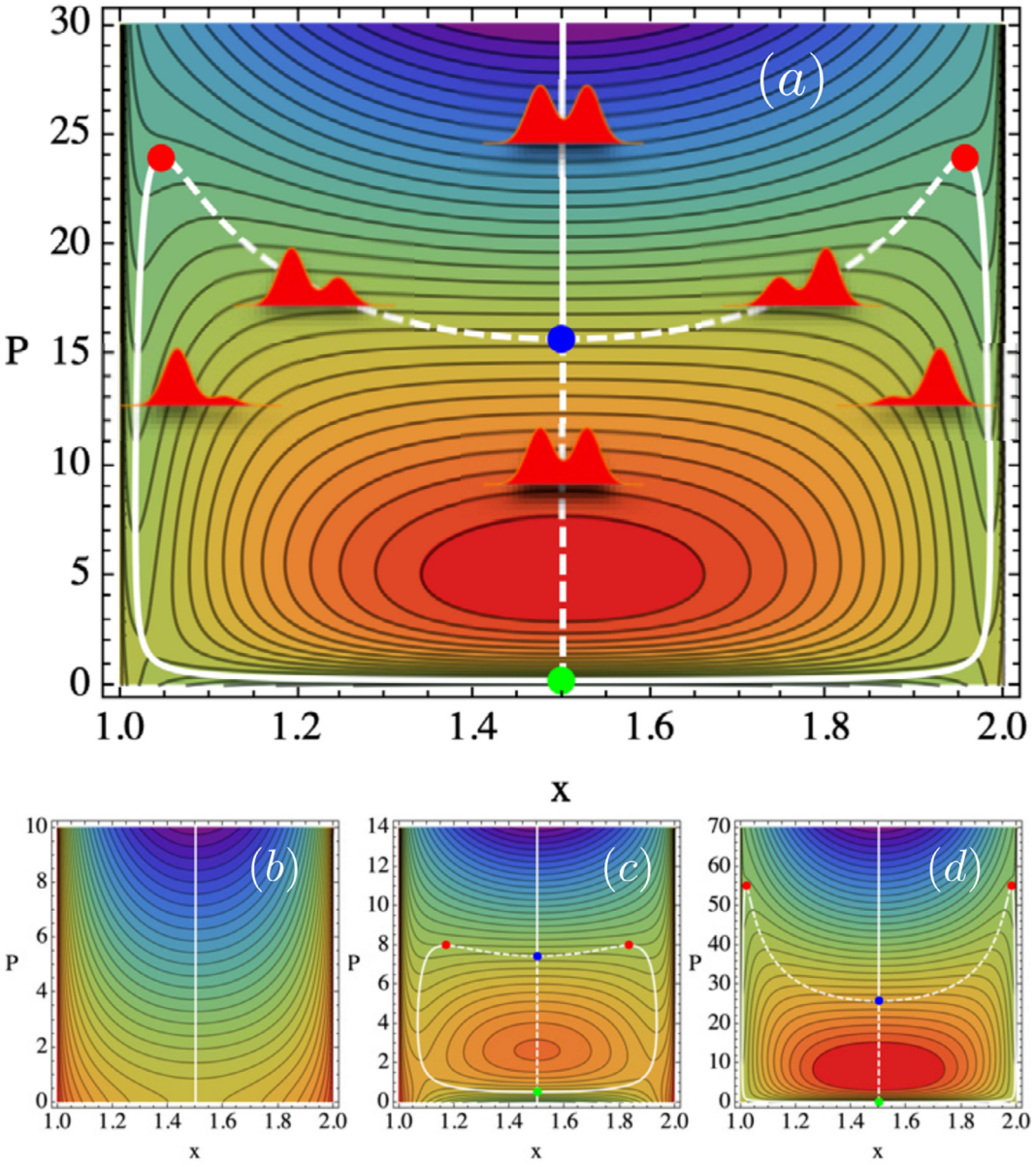

Fig. 2. Contour plots for effective potential $H(x, P)$ for different values of γ: (a) 10, (b) 2, (c) 6, and (d) 15. $V = 1$. Color dots are explained in the text. Full (dashed) lines correspond to stable (unstable) stationary solutions. The color scale is *rainbow*, with purple-blue (red) indicating lower (larger) values, with green intermediate values. Insets in (a) show some spatial profiles at different x-values. (For interpretation of the references to colour in this figure legend, the reader is referred to the web version of this article.)

center of mass is simply defined as $x \equiv 1 + \bar{x}$. $\bar{x} = 0$ $(x = 1)$ means that all the power is at waveguide 1 $(P = P_1)$, while $\bar{x} = 1$ $(x = 2)$ indicates that all the power is at waveguide 2. $\bar{x} = 0.5$ $(x = 1.5)$ represents both, the $++$ and $+-$ solution; however, as $\gamma > 0 \Rightarrow \alpha > 0$, we are only interested on the connection of nontrivial solutions with symmetric $(++)$ modes.

To characterize the dynamical features of this system, we construct an effective potential $H(\bar{x}, P)$. From the definition of $\bar{x}$, we write $u_1 = \sqrt{P(1-\bar{x})}$ and $u_2 = \sqrt{P\bar{x}}$, in which we have selected positive signs due to the focusing nonlinearity and the unstaggered nature of solutions. Inserting these expressions into Eq. (3), we get a simple form for the effective potential

$$H(\bar{x}, P) = -2VP\sqrt{\bar{x}(1-\bar{x})} + \gamma \log[1 + P + P^2\bar{x}(1-\bar{x})]. \quad (6)$$

We plot a normalized effective potential in Fig. 2(a) for $\gamma = 10$, as an example, as a function of x and P. To simplify the comparison at different P values, we have normalized $H(x, P)$ diving it by $H(0, P)$, to rescale values and simplify the analysis. We have also included examples in Figs. 2(b)–(d) for other values of γ, to compare main phenomenological changes.

Critical points of $H(x, P)$ are found directly from expression (6), obtaining the nonlinear stationary solutions connected in parameter space (antisymmetric solution $+-$ is dynamically isolated for $\gamma > 0$). A first solution corresponds to the *symmetric* one, for which $\bar{x}_{sym} = 0.5$. This mode exists for all powers, bifurcating at zero power for $\lambda = V - \gamma$ and disappearing at an infinite power for $\lambda = V$. The central vertical curve in Fig. 2 illustrates this symmetrical state. Its stability properties change depending on the level of power and emergence of nontrivial solutions $\alpha_{\pm}$. For $\gamma < 4$, the symmetric solution is always a minimum, been therefore always stable. For $\gamma > 4$, it evolves from been a minimum into a maximum and into a minimum again, modifying its stability conse-

quently. After differentiating expression (6), we obtain two nontrivial solutions

$$\bar{x} = \frac{1}{2} \pm \frac{1}{2}\sqrt{1 - \frac{2}{P^2V^2}\, y_{\pm}}, \tag{7}$$

with $y_{\pm} = \gamma^2 - 2(1+P)V^2 \pm \gamma\sqrt{\gamma^2 - 4(1+P)V^2}$, which are located symmetrically around the symmetric solution ($\bar{x} = 0.5$). These nontrivial solutions are spatially asymmetric in terms of amplitudes at each waveguide ($\alpha_{\pm} \neq 1$) and are phenomenologically connected to localized nonlinear solutions of extended systems [17–19]. Considering their profile, we simply call them *asymmetric* modes. Expression (7) imposes restrictions for analytical solutions, considering that $\bar{x}$ is a real quantity. The first condition we observe is that these solutions do not exist above the upper bound $P_{ub} = (\gamma/2V)^2 - 1$ (red dots in Fig. 2). Therefore, the condition $\gamma > 2V$ is necessary in order to have asymmetric nonlinear solutions (same condition is obtained when looking for opening a "*gap*" in between linear modes: $V - \gamma < -V$, which is a region in parameter space where localized solutions exist [17–19]). Fig. 2(b) shows that there is only one stationary solution for $\gamma = 2V$, the symmetric mode. For $P > P_{ub}$, only symmetric (and antisymmetric) solutions exist, which is a signature of the saturable nonlinearity and its tendency to become a linear system at high powers.

Additionally, we find two extra conditions which define the bifurcation power for two different asymmetric solutions: $P_{\pm} = \gamma/V - 2 \pm \sqrt{(\gamma/V-2)^2 - 4}$. Power P_{-} represents the bifurcation power for a standard asymmetric solution, similar to the one found for a nonlinear cubic dimer [10]. Around this parameter region, saturable phenomenology approaches to the nonlinear cubic one, as we have described before. This new stable solution bifurcates at P_{-} from the symmetric mode, which now becomes unstable: a minimum is transformed into a maximum in the effective potential representation. This bifurcation power is indicated by green dots in Figs. 2(a), 2(c) and 2(d), been: 0.25, 0.54, and 0.15, respectively. Because of the system symmetry, the asymmetric solution exist to the right and to the left of $\bar{x} = 1/2$ [using y_{-} in Eq (7)], positions that correspond to two local minima in the potential representation. Therefore, this asymmetric mode is always stable in its whole existence region: $\{P_{-}, P_{ub}\}$, denoted by full lines in Fig. 2.

Interestingly, an extra mode appears for a saturable system at P_{+} [replacing y_{+} in Eq (7)], which is a fundamentally different result compared to a standard cubic dimer. For cubic nonlinearities, the asymmetric mode exists from a given power threshold $2V/\gamma$ up to infinity, without any fundamental change in its dynamical properties. However, for a saturable dimer, a second asymmetric solution appears at power P_{+} (see blue dots in Fig. 2). This solution is a connector mode or *intermediate* solution in between the symmetric mode and the first stable asymmetric state. This solution appears as a maximum in the potential representation, been always an unstable solution in its existence region $\{P_{+}, P_{ub}\}$ and, therefore, a new hyperbolic point for the system. Because of the appearance of this second asymmetric state, the symmetric mode becomes stable in the interval $\{P_{+}, \infty\}$. Consequently, we observe a bistable regime where the symmetric and first asymmetric modes are simultaneously stable, been both equilibria in the system for the same level of power.

In brief, as a function of the power P and strength of saturation γ, the optical dimer presents regions of monostability and bistability. These bistability regions appear and disappear due to pitchfork and saddle-node bifurcations, as illustrated in Fig. 2.

3. Dynamic for an integrable dimer

We numerically integrate the set of Eq. (1), assuming a given input condition, and study the dynamics of the optical dimer using two methods. The first one consists of computing the spectrum excited along the propagation coordinate z [23], which gives us information about the frequencies effectively excited or frequencies decomposition during the dynamics for a different level of power. We run the simulations up to a given propagation distance $z_{\max}$, long enough to allow the different frequencies to emerge. Figs. 3(a) and 3(b) show two examples, for $\gamma = 10$, where we excite the system using a single-site and two-sites (symmetric) excitation, respectively.

First of all, considering the excitation of a single waveguide [Fig. 3(a)], we observe that for a low power regime both linear frequencies are excited [see Fig. 3(a2)]. This is due to the excitation of both linear eigenmodes simultaneously: "+0" = "++" + "+−"; i.e., a single-site excitation. As the nonlinearity is positive, frequencies are shifted to the right of the spectrum for an increasing power, where the $\gamma + V$ symmetric mode is mostly excited. However, there is an oscillation of the energy from one site to the other as Fig. 3(a3) shows. For $P \gtrsim 1$, the center of mass shrinks and $x \to 1$; i.e, the energy remains trapped at the input waveguide. This is the well-known self-trapping transition [9,10,13,15,23–25], which occurs above a given level of power. As it was shown in Fig. 2, the asymmetric stationary mode bifurcates from the symmetric state, which is corroborated dynamically in Fig. 3(a). Once the asymmetric mode is excited, it governs the dynamics and the strong peak in the spectrum corresponds to this state, with only few energy been transferred into the second waveguide. Indeed, a single-site excitation does not match exactly to the asymmetric stationary mode; therefore, some part of the energy oscillates in between both waveguides. As the effective potential (6) predicts, there is a second bifurcation region which modifies the system dynamics. Close to power P_{+} (15.746, for $\gamma = 10$) there is a regime where saturation emerges and stabilizes the previously unstable symmetric solution. Therefore, as the input condition corresponds to $x(0) = 1$, there is a transit in between two minima which induces an oscillation of the center of mass as shown in Fig. 3(a3). This oscillation continues for an increasing power, where for $P > P_{ub}$ only the symmetric mode is excited because is the only remaining stationary solution at larger power.

Fig. 3(b) shows similar diagrams but for a symmetric input condition $x(0) = 1.5$. For low level of power, we observe how the symmetric mode rapidly unstabilizes and generate several harmonic as shown in Fig. 3(b2). This is corroborated with the oscillation of x shown in Fig. 3(b3) for low powers. Then, above $P \approx 16$, the symmetric solution stabilizes, that is, no harmonic are generated [see Fig. 3(b2)] and the center of mass oscillation ends [see Fig. 3(b3)].

A second method corresponds to a Poincaré map [22], which helps us to understand the overall system dynamics for longer propagation distances. This is necessary to allow the energy to explore the full parameter space (initial conditions), in order to show different stable equilibria and hyperbolic points. To implement this map in our system, we construct a parameter space formed by the center of mass $x(z)$ and its derivative

$$dx \equiv \frac{dx}{dz} = \frac{-2\mathrm{Im}(u_1 u_2^*)}{P}, \tag{8}$$

where dx indicates a transversal velocity for which the center of mass x changes along the propagation coordinate. As stationary solutions are naturally immobile, parameter space must show these points as equilibrium and isolated points in the map. To construct these diagrams, we initialize Eq. (1) using $N = 101$ input conditions, which go from $x(0) = 1$ to $x(0) = 2$ as $x(0) = 1 + (j-1)/(N-1)$, with $j = 1, \ldots, N$. Color code in Poincaré maps correspond to a rainbow scheme, where red/orange increases up to blue/purple, passing through greenish colors, for an increasing j-value.

Fig. 4 presents four different examples at different level of power to show the different phenomenological regimes for this

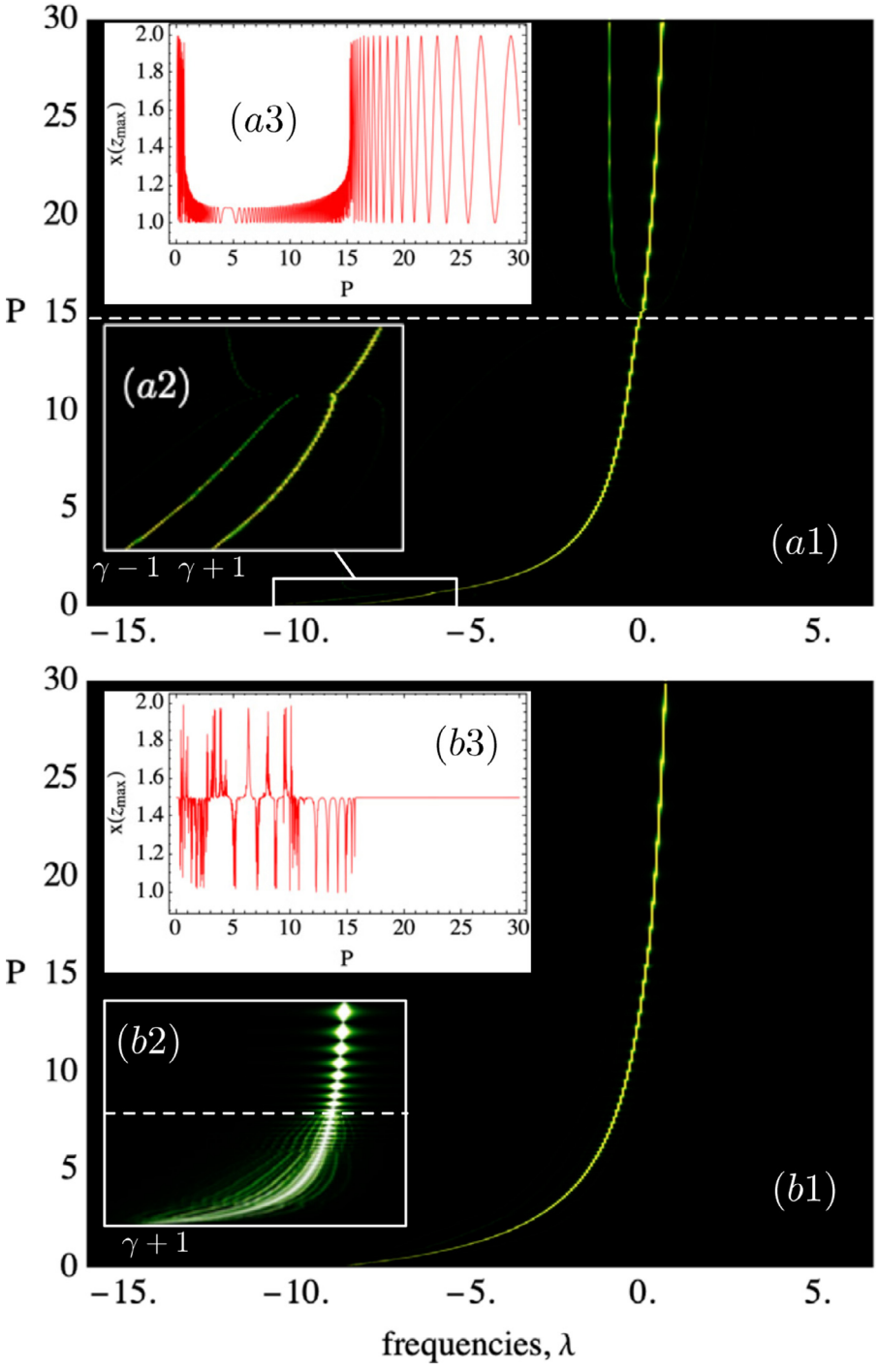

Fig. 3. Optical dimer dynamics for input excitation (a) $x(0) = 1$ and (b) $x(0) = 1.5$. (a1) and (b1) Dynamically excited spatial frequencies λ are plotted for different input power P. (a2) zoom of (a1) at indicated region, while (b2) shows (b1) on a saturated scale. (a3) and (b3) show $x(z_{\max})$ versus input power P. Dashed lines indicates $P = 15$. $V = 1,\ \gamma = 10,\ z_{\max} = 100$.

system. At low power [see Fig. 4(a) for $P = .1$], we observe a single fixed point at $x = 1.5$, which corresponds to the symmetric stable solution, i.e. an isolated center equilibrium. All orbits around it describe a closed trajectory, indicating an oscillating behavior for any input condition different to $x = 1.5$. For powers in the interval $\{P_-, P_+\}$, the symmetric solution becomes unstable and transforms into an hyperbolic point at $x = 1.5$, while the asymmetric modes emerges as new center points [see Fig. 4(b) for $P = 10$]. In Fig. 2(a) we see that, when bifurcating, the asymmetric solution rapidly modifies its center of mass close to waveguides 1 and 2. In fact, for $P > 1$, the shift in position (with respect to waveguides) is less than 0.02. For $P = 10$, stationary solutions are located in $x = 1.016$ and $x = 1.984$ [obtained directly from expression (7)], corresponding to the two fixed points shown in Fig. 4(b). All this dynamics is well-known and identical to the one for the cubic dimer [9–11].

For powers in the interval $P_+ < P < P_{ub}$, we expect that saturation starts affecting the dynamics. In this parameter region, we expect to observe three fixed points: two stable asymmetric solutions around a third stable symmetric solution at $x = 1.5$. In addition, we naturally expect two hyperbolic points connecting the sta-

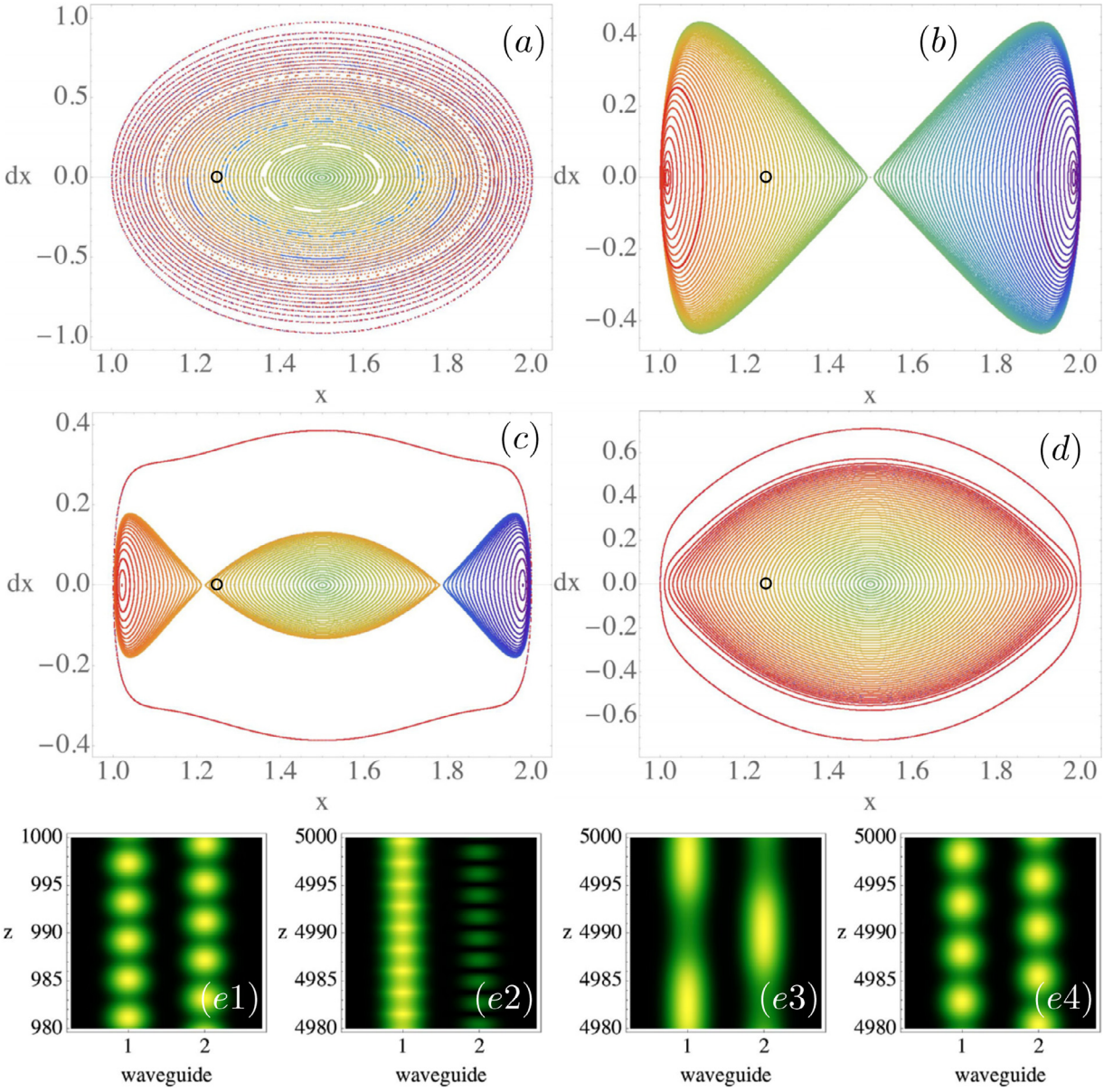

Fig. 4. Poincaré maps, phase space $\{x, dx\}$, for different power P: (a) 0.1, (b) 10, (c) 18, and (d) 30. $V = 1$, $\gamma = 10$, $z_{\max} = 1000$ for (a) and 5000 for (b)–(d). (e1)–(e2) Waveguide power $|u_{1,2}(z)|^2$ at the last part of propagation for (a)–(d) cases, respectively, with $x(0) = 1.25$ as indicated by black circles.

ble modes. Fig. 4(c) shows this phenomenology for $P = 18$, where fixed points are located at $x = 1.02$, 1.5, and 1.98, while hyperbolic points at $x = 1.22$, and 1.78. Finally, for $P > P_{ub}$ we expect to observe a kind of linear behavior, due to the saturation and disappearance of asymmetric solutions. The only stationary solution remaining corresponds to the symmetric one, been therefore an isolated fixed point. This is well described in Fig. 4(d) for $P = 30$. Figs. 4(e1)–(e2) show some dynamical examples at the end of the computed trajectory, where regular and predictable oscillatory behavior is observed in all cases for the same input condition, but for different power and, therefore, different dynamical regimes.

When the optical dimer presents bistability between different stable equilibria, their stability regions are circumscribed by the heteroclinic and homoclinic orbits [22], as shown in Figs. 4(b) and 4(c). These orbits are generated from the hyperbolic points and connections between them. The chaos theory initiated by the pioneering works of Poincaré shows that disturbances of a dynamical system, for example periodic forcing, induce chaotic behaviors around heteroclinic and homoclinic curves [22].

4. Chaos on a saturable optical dimer

In order to observe a chaotic dynamics on a dimer system, we must introduce an external driving that turns model (1) into a non-integrable system. Namely, we must remove a conserved quantity. In a photonic platform, we could induce parametric changes by varying fabrication parameters. Coupling V can be spatially modulated by changing the distance in between waveguides, and nonlinearity γ can be adjusted as well by varying the pulse energy of the femtosecond laser used for waveguide writing [16]. However, this technique is implemented in silica-like materials which have a nonlinear cubic response. Saturable systems are commonly studied on photorefractive materials, for example a SBN crystal [15]. The nonlinear coefficient γ can be controlled by an external voltage applied on one crystal axis, which allows the study of linear and nonlinear dynamics at a very low level of optical

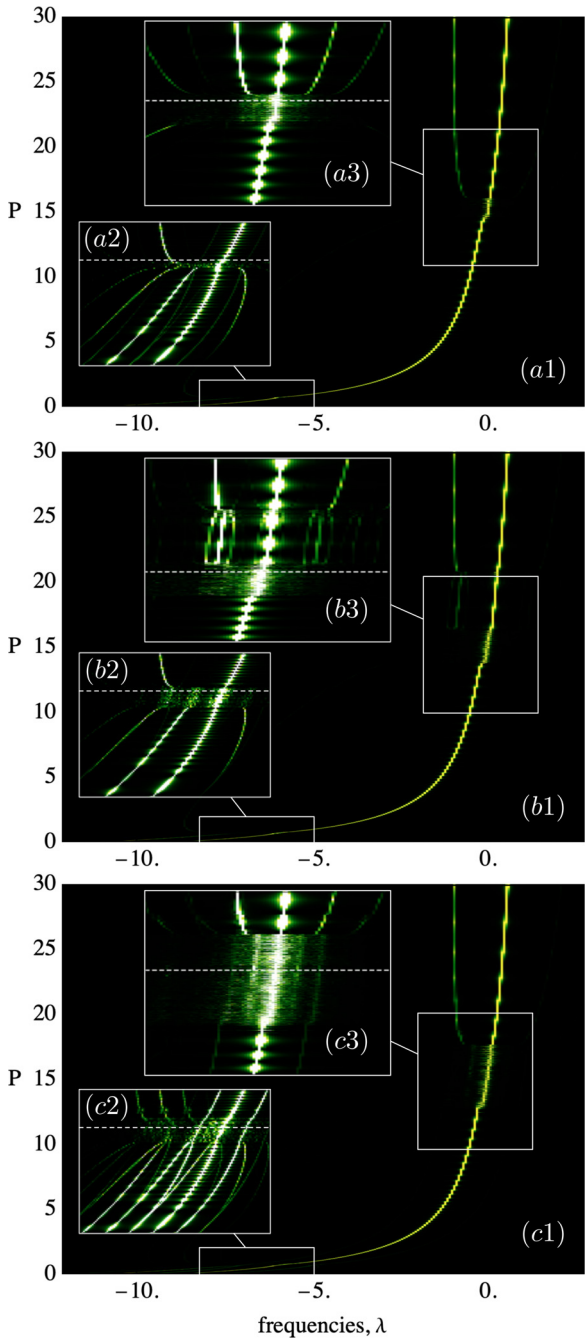

Fig. 5. (a), (b) and (c) Dynamically excited spatial frequencies λ as a function of input power P, for a single site excitation $x(0) = 1$, for $\{\gamma_1, \omega\} = \{0.2, 1\}$ (a), $\{0.2, 2\}$ (b), and $\{1, 1\}$ (c). (a1) shows the excited spectrum for $P \in \{0, 30\}$, normalized with the maximum peak at every P. (a2), (b2) and (c2) show zooms at bifurcation power region P_{-}, while (a3), (b3) and (c3) at the multi-stable region $\sim \{P_{+}, P_{ub}\}$, both on a saturated scale. $V = 1,\ \gamma_0 = 10,\ z_{\max} = 100$.

power. As this voltage is externally applied, it can be varied on a controlled oscillatory way. Therefore, we can study the effect of having an oscillatory nonlinearity on model (1), for which we consider

$$\gamma \to \gamma(z) = \gamma_0 + \gamma_1 \sin(\omega z). \tag{9}$$

Following previous analysis, we take $\gamma_0 = 10$ and vary γ_1 and ω as control parameters in order to study the emergence of chaos. First of all, we compute the frequency spectrum for different input conditions. Fig. 5 summarizes the obtained results. Along this section, we consider three cases as examples: a weak-slow (*ws*) $\{\gamma_1, \omega\} = \{0.2, 1\}$, a weak-fast (*wf*) $\{\gamma_1, \omega\} = \{0.2, 2\}$, and strong-slow (*ss*) $\{\gamma_1, \omega\} = \{1, 1\}$ perturbations. Our idea is to see the main effects of varying the strength and frequency of nonlinear modulation. Naturally, Figs. 5(a1)–(c1) show a similar result than the one shown in Fig. 3(a), where we observe the four main regimes: excitation of low-power symmetric and antisymmetric modes, bifurcation of asymmetric solutions, multi-stable region, and excitation of high-power symmetric and antisymmetric modes again. However, if we zoom up the dynamically more interesting regions [low power at Figs. 5(a2),(b2) and (c2), and intermediate power Figs. 5(a3), (b3) and (c3)], we realize that the nonlinear modulation introduces the generation of new harmonics which could be of great relevance for perturbing the stability and propagation of different input conditions. These figures are color saturated in order to show more details in the spectrum, although these details are weak with respect to main frequencies.

We nicely observe how the nonlinear modulation destabilizes the region where transitions are happening: $P \sim P_{-}$ and $P \sim \{P_{+}, P_{ub}\}$, generating a kind of continuous excitation of frequencies in the transitions regions. We notice that this continuous generation increases in terms of affected power interval for an increasing modulation from *ws* $\to$ *wf* $\to$ *ss*, in both power regimes. Therefore, we expect a more chaotic scenario for an increasing forcing of the system. However, although this is an obvious conclusion, we also notice that when power is above $P \sim P_{ub}$, system stabilizes again without any relevant harmonic generation and observed instability. On the contrary, we observe a high-power linear regime, which is a saturable signature, been completely different to the standard cubic phenomenology ocurring at larger power levels.

To deepen the analysis, we construct different Poincaré maps (following the same scheme than in the previous section in terms of input conditions) at different level of power, for the same three different nonlinear modulation parameters (*ws, wf*, and *ss* regimes), in which each point of the phase space $\{x, dx\}$ is obtained stroboscopically after a period $T = 2\pi/\omega$. Fig. 6 shows results for $P = 10$ after propagating the equations up to $z_{\max} = 5000$ [different colors represent a different input conditions from $x(0) = 1.0$ (red) to $x(0) = 1.5$ (violet)]. At this level of power, we expect a system presenting two fixed and one hyperbolic points as shown in Fig. 4(b). For a soft modulation (*sw*), Fig. 6(a) shows the broadening of the region close to the original hyperbolic point at $x = 1.5$ (green colors). This is a clear manifestation of the chaotic behavior that emerges from the explosion of the homoclinic curve, *homoclinic entanglement* [7,22]. Therefore, an initial condition in this region of the phase space is exponentially sensitive; if one starts from an almost symmetric initial condition, after evolving, it will not be possible to predict whether the light intensity is concentrated in the left or the right waveguides. Although the trajectories tend to mix in this region, their size is small. Indeed, the chaotic region is a delimited zone of phase space, which is fractal in nature [7].

By inspecting three specific input conditions [black curves in Figs. 6(d)–(f)], we observe that close to the original fixed point (triangle and circle) the energy remains oscillating stable around this point. However, close to the hyperbolic point (square, chaotic region), we observe that the energy goes back and forward from sites 1 and 2, which is in agreement with the broadening of the greenish region. Fig. 6(b) shows an essentially similar result than Fig. 6(a); however, we observe that the previously chaotic (green) region starts to become mixed with orange and blue colors. This is an indication of a chaotic tendency due to the effective connection of trajectories for different input conditions. Blue curves in Figs. 6(d)–(f) show this, where for $x(0) = 1.1$ there is a stable oscillatory trajectory, but for $x(0) = 1.3$ there is a jump into waveguide two and then back to waveguide one again. Hence, in the last case the trajectory is not bounded to the left fixed point

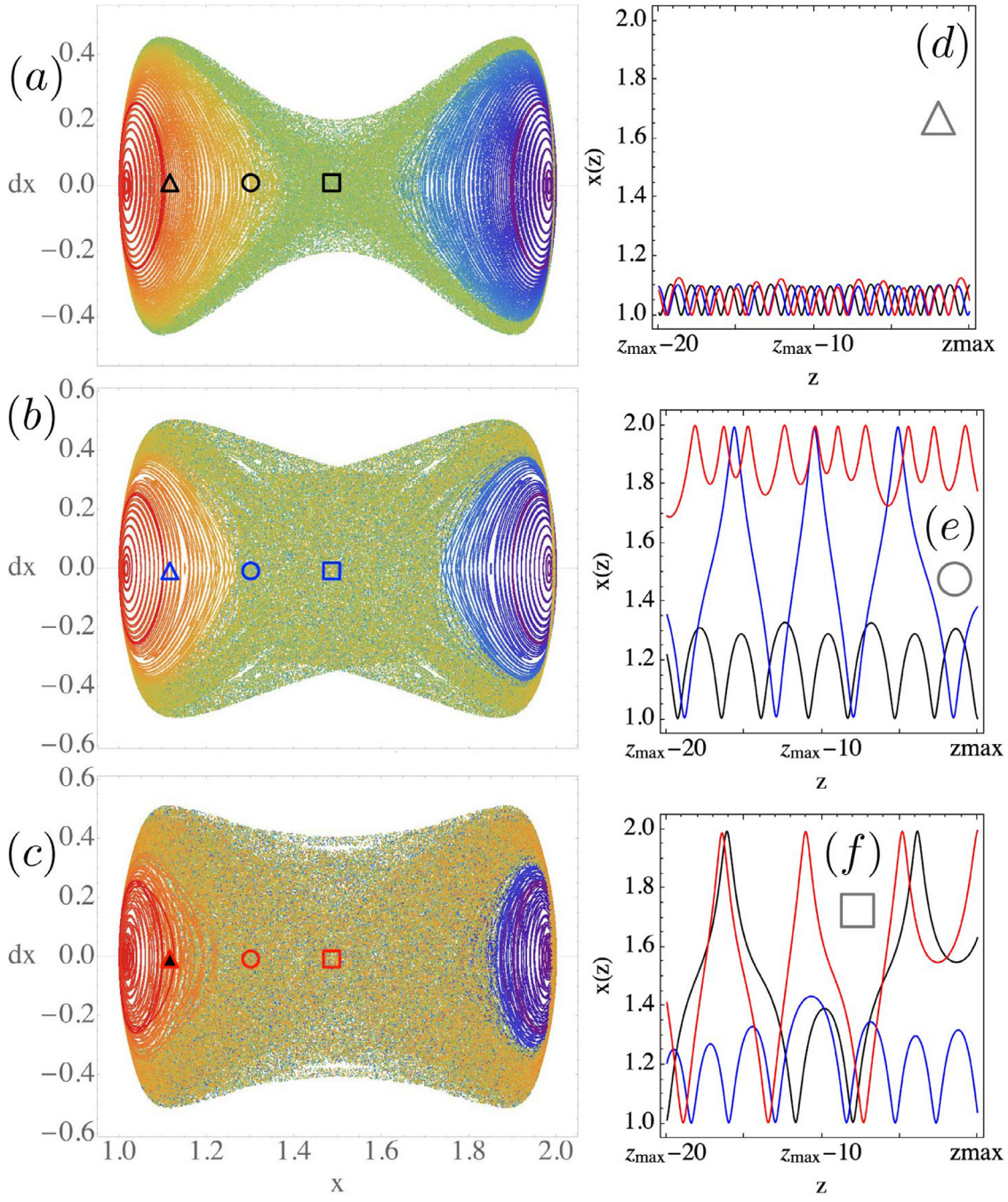

Fig. 6. Poincaré maps for power $P = 10$ and $\{\gamma_1, \omega\} = \{0.2, 1\}$ (a), $\{0.2, 2\}$ (b), and $\{1, 1\}$ (c). (d), (e) and (f) show $x(z)$ at the end of propagation, for input conditions $x(0) = 1.1$ (d), 1.3 (e), and 1.49 (f), as indicated by triangles, circles and squares, respectively. Black, blue, and red curves correspond to the same parameter used in (a), (b), and (c), respectively. $V = 1,\ \gamma_0 = 10,\ z_{max} = 5000$. (For interpretation of the references to colour in this figure legend, the reader is referred to the web version of this article.)

and goes back and forward from one site to another. Then, for an input condition closer to the hyperbolic point [$x(0) = 1.49$], we observe in Fig. 6(f) that energy got trapped at the left fixed point and remains oscillating around it, although this is not a stable observation as it is shown around $z = z_{max} - 10$, where it was close to jump into the other site, something that probably happens before or will occur afterwards. Finally, for this level of power, a *ss* regime shows a strong mix of trajectories in Fig. 6(c). We observe a clear emergence of fully developing chaos, where essentially only red and violet trajectories at the left and right fixed points, respectively, are stable, as Fig. 6(d) shows by red lines. Likewise, when the input condition moves away from fixed points, trajectories are simply chaotic and the energy goes back and forward in a non trivial way [see red lines in Figs. 6(e) and (f)].

All the described phenomenology is akin to the cubic dimer one, because at this level of power the system behaves as a Kerr system. The saturable nature of our model appears in the multistable regime, for example as shown in Fig 4(c). There, three fixed and two hyperbolic points define a completely different scenario. Fig. 7 shows our compiled results for $P = 18$, and *ws*, *wf*, and *ss* regime. In the first two regimes, we observe a kind of similar result, but presenting different patterns at the Poincaré section. Close to the three fixed center points, there are stable trajectories as shown in Figs. 7(a) and (b), by red, green and violet colors. These

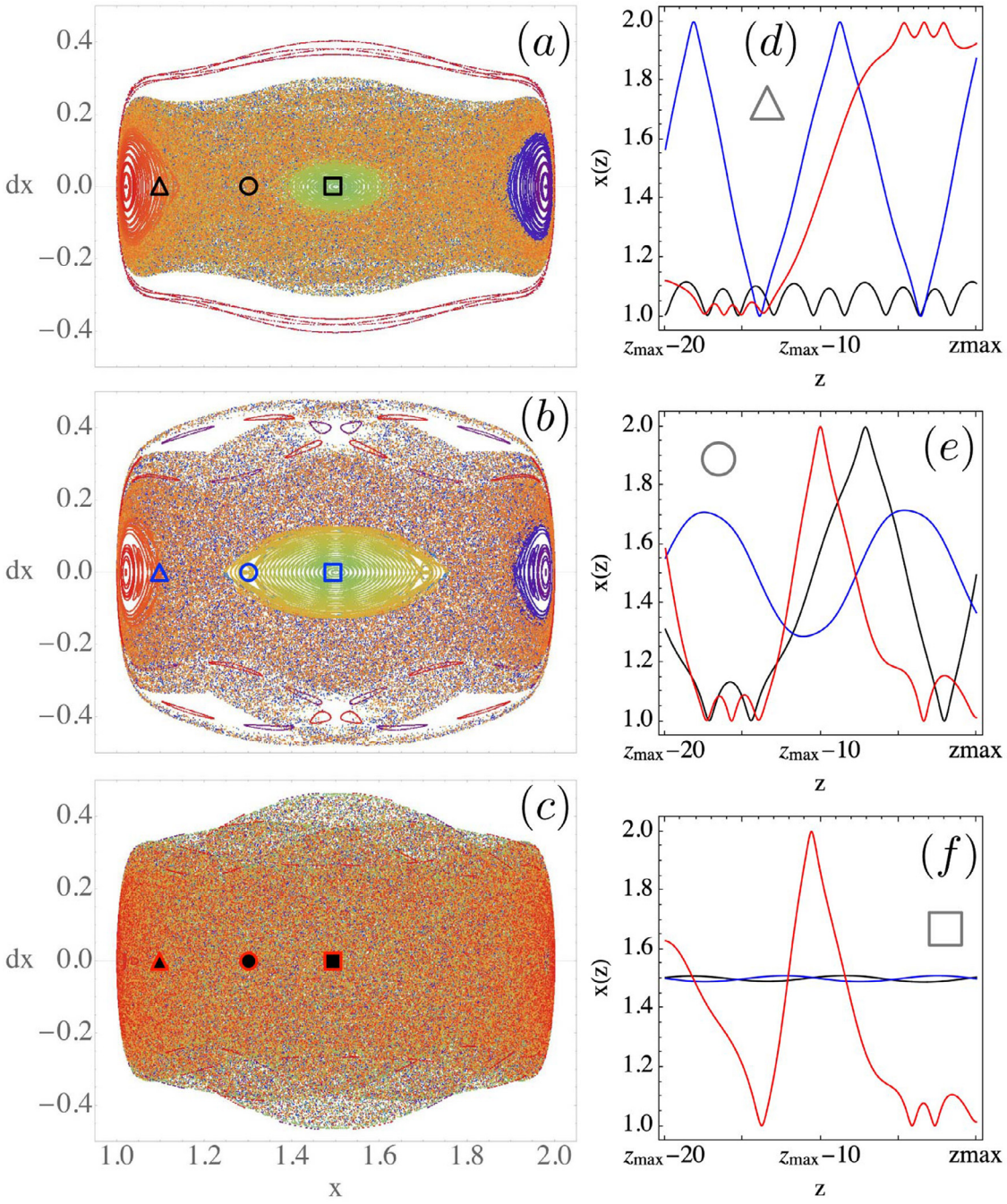

Fig. 7. Poincaré maps for power $P = 18$ and $\{\gamma_1, \omega\} = \{0.2, 1\}$ (a), $\{0.2, 2\}$ (b), and $\{1, 1\}$ (c). (d), (e) and (f) show $x(z)$ at the end of propagation, for input conditions $x(0) = 1.1$ (d), 1.3 (e), and 1.49 (f), as indicated by triangles, circles and squares, respectively. Black, blue, and red curves correspond to the same parameters used in (a), (b), and (c), respectively. $V = 1,\ \gamma_0 = 10,\ z_{\max} = 5000$. (For interpretation of the references to colour in this figure legend, the reader is referred to the web version of this article.)

regions of the phase space are characterized by the fact that the trajectories can be foliated (islands), whereas in chaotic regions this is not possible. In the *ws* regime, we observe a clear separation of dynamics. We observe how for an input condition $x(0) = 1.1$, at weak modulation (*ws*), trajectory is stable around the left fixed point as black lines show in Fig. 7(d). However, when increasing the input condition to $x(0) = 1.3$, we observe a mixed dynamics in Fig. 7(a), which is an indication of chaos, where the energy goes back and forward in a non trivial form [see black curve in Fig. 7(e)]. Then, close to the new fixed point [$x(0) = 1.49$], we observe a perfectly bounded trajectory in Fig. 7(f), for both, *ws* and *wf*, regimes, shown by black and blue curves, respectively. Coming back to $x(0) = 1.3$, but now for a *wf* regime, we observe a bound and stable oscillation in turn the central fixed point [see blue curve in Fig. 7(e)]. Interestingly, the same input condition in a *ws* regime indicated chaos. Therefore, we observe how a faster modulation induces a new control of stable trajectories, where the central stable region around the fixed point $x = 1.5$ has increased. However, an input condition $x(0) = 1.1$ shows a not bounded trajectory, with the energy oscillating from one site to the other [see blue curve in Fig. 7(d)]. In a *wf* regime, we observe that the region in between fixed points is more colored, with almost all colors mixed in phase

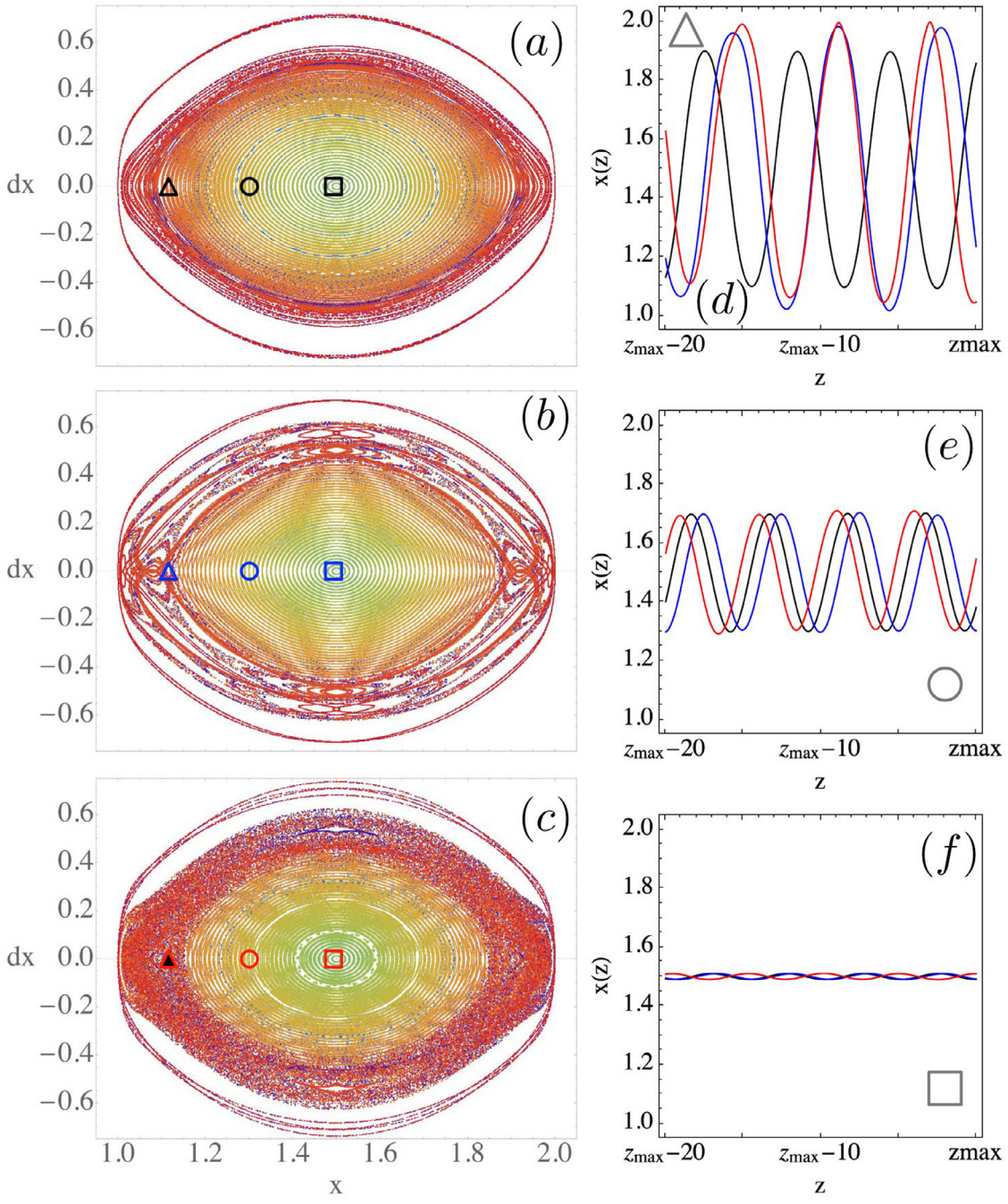

Fig. 8. Poincaré maps for power $P = 30$ and $\{\gamma_1, \omega\} = \{0.2, 1\}$ (a), $\{0.2, 2\}$ (b), and $\{1, 1\}$ (c). (d), (e) and (f) show $x(z)$ at the end of propagation, for input conditions $x(0) = 1.1$ (d), 1.3 (e), and 1.49 (f), as indicated by triangles, circles and squares, respectively. Black, blue, and red curves correspond to the same parameters used in (a), (b), and (c), respectively. $V = 1$, $\gamma_0 = 10$, $z_{\max} = 5000$. (For interpretation of the references to colour in this figure legend, the reader is referred to the web version of this article.)

space, what is a clear manifestation of chaos. We also observe the appearance of isolated closed trajectories ("islands"), as an indication of a periodic dynamics; however, these trajectories are not reached by trivial input conditions, considering that we can only set the input center of mass in an experiment. Finally, we observe that a strong modulation (*ss*) regime, at this level of power, only shows a chaotic behavior, with the whole phase space covered by mixed trajectories. Examples are shown by red lines in Figs. 7(d)–(f), where we observe a non trivial dynamics with exchange of energy between sites and kind of short bound oscillation around left and right fixed points.

Finally, to show the saturable nature of our model Eq. (1), we increased the power up to $P = 30$, where saturation comes into play and determine the dynamics with an isolated fixed point at $x = 1.5$, as shown in Fig. 4(d). In this regime, the dynamics is governed by symmetric and antisymmetric solutions only, which are the only fixed points in a high-power linear regime. Therefore, we mostly observe oscillation in turn this fixed point, as shown in Figs. 8(a)–(c) for $x(0) = 1.3$ (circles) and $x(0) = 1.49$ (squares), with simple oscillatory dynamics and a well defined period [see Figs. 8(e) and (f)]. Dynamics becomes more complex close to the previous left and right fixed points, which now do not exist any-

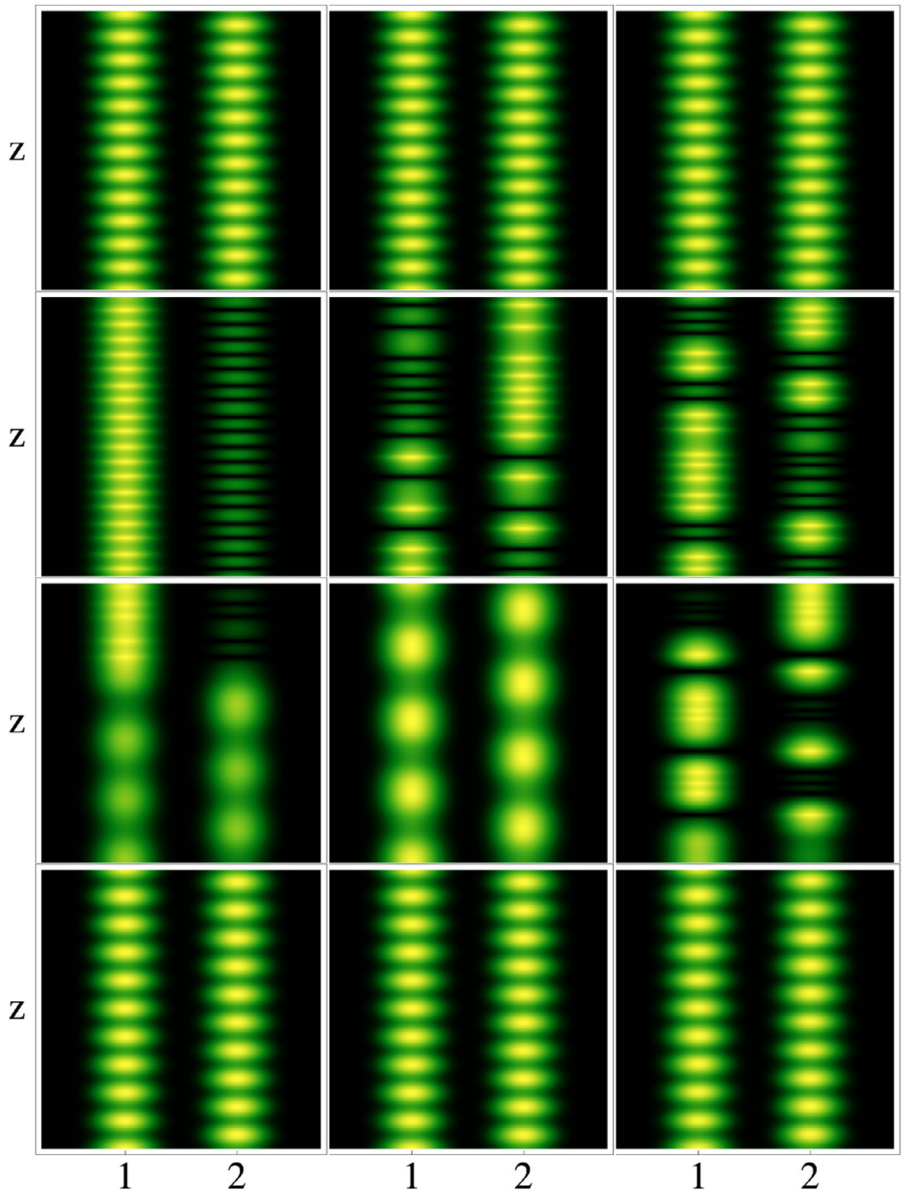

Fig. 9. Dynamical examples for an input excitation $x(0) = 1.1$. Four files correspond to powers $P = .1,\ 10,\ 18,\ 30$, while three columns correspond to $\{\gamma_1, \omega\} = \{0.2, 1\}$, $\{0.2, 2\}$ and $\{1, 1\}$, respectively. $V = 1,\ \gamma_0 = 10,\ z_{\max} = 50$.

more, but we find a non simple dependence in the effective potential at this region, as shown in Fig. 2(a). Derivative at these regions change, although no critical points (hyperbolic or center points) are found, but inflection points. We observe this complexity for an input condition $x(0) = 1.1$ in all regimes, where we nevertheless observe a quite periodic, but not trivial, oscillation, as shown in Fig. 8(d). Islands appear at intermediate and strong regimes, with some chaotic mixing regions in between those islands. This is an interesting feature of this model, because although stationary solutions at this level of power behave as linear ones, they are still nonlinear effects which could manifest chaos as we clearly show, for example, in Fig. 8(c), where there is a broad chaotic region with several colors mixed. Only single-site input conditions could circulate through the system without noticing the effective potencial, as shown in Figs. 8(a)–(c) by broader trajectories which mix red and violet colors only.

5. Conclusions and remarks

Coupled waveguides as a function of the initial condition and power of the injected light exhibit complex dynamic behaviors. We show that simply considering a saturable optical dimer with spatial modulation exhibits chaotic behaviors. By using frequency spectra and Poincare sections, we give evidence of the complex dynamics exhibited by this simple system. Because of the saturable nonlinearity that characterizes the optical dimer under study, chaotic behaviors are exhibited only in an intermediate power range. The origin of the chaotic behavior is due to the entanglement of the homoclinic and heteroclinic curves associated with the hyperbolic points that separate the stable equilibria of the saturable optical dimer.

Using our previous findings, we would like to explore a possible application considering the saturable properties and the activation of chaotic dynamics using an external driving mechanism. Nowadays, the encrypted transmission of information is a key goal

for increasing digital demand, including different transactions requiring a high degree of security. Hence, the ability to send information in a codified way is mandatory. Our saturable system has the particularity of presenting linear regimes at different levels of power and, therefore, we could have a controlled output below and over a defined power threshold, while having a chaotic and hard to predict regime at an intermediate level of power. As this system has only two degrees of freedom, the energy could only transit from one site to another, but the output could change abruptly on a chaotic regime. This could be interpreted as a non-controlled output for an eavesdropper, for example. This is similar to the Alice and Bob idea on quantum information [26], and as soon as the emitter and receiver knows the correct protocol, in our case defined with the level of power used in the system, the information will be securely transferred.

Fig. 9 shows some examples, varying different parameters, power P in rows and $\{\gamma_1, \omega\}$ in columns. As we clearly observe, low and high power regimes show a controlled oscillatory output, but intermediate powers show a non periodic dynamics which could produce confusion on an eavesdropper. As the system tends to be chaotic in an intermediate power regime, this produces periodic and non-periodic output patterns which could be really hard to predict due to the non-integrability of model (1) + (9). Therefore, we can use the chaotic regime to occult information, considering the optical power as external control of the system. Work in this direction is in progress.

This work was supported in part by Millennium Science Initiative Program ICN17_012 and FONDECYT Grants 1191205 and 1210353.

Declaration of Competing Interest

The authors declare that they have no known competing financial interests or personal relationships that could have appeared to influence the work reported in this paper.

References

[1] Frova A, Marenzana M. Thus spoke galileo: the great Scientist's ideas and their relevance to the present day. New York: Oxford University Press; 2006.
[2] Baker GL, Blackburn JA. The pendulum: A Case study in physics. Oxford University Press; 2005.
[3] Nayfeh AH, Mook DT. Nonlinear oscillations. New York: John Wiley & Sons, Inc; 1980.
[4] Shinbrot T, Grebogi C, Wisdom J, Yorke JA. Chaos in a double pendulum. Am J Phys 1992;60:491.
[5] Landau LD, Lifchitz EM. Mechanics. Burligton: Pergamon Press; 2003.
[6] Guckenheimer J, Holmes P. Nonlinear oscillations, dynamical systems and bifurcations of vector fields. New York: Springer-Verlag; 1983.
[7] Jackson EA. Perspectives of nonlinear dynamics: volume 1. Cambridge: Cambridge University Express; 1989.
[8] Fusco C, Fasolino A, Janssen T. Nonlinear dynamics of dimers on periodic substrates. Eur Phys J B 2003;30:95.
[9] Ou BY, Zhao XG, Chen SG. Dynamic transition and chaotic behavior in a nonlinear dimer driven by a laser field. Physica B 1999;269:145.
[10] Hennig D, Esser B. Transfer dynamics of a quasiparticle in a nonlinear dimer coupled to an intersite vibration: chaos on the bloch sphere. Phys Rev A 1992;46:4569.
[11] Hennig D, Mulhern C, Burbanks AD. From strong chaos via weak chaos to regular behaviour: optimal interplay between chaos and order. Physica D 2013;253:102.
[12] Jensen SM. The nonlinear coherent coupler. IEEE J Quantum Electron 1982;18:1580.
[13] Guzmán-Silva D, Lou C, Naether U, Rüter CE, Kip D, Vicencio RA. Multistable regime and intermediate solutions in a nonlinear saturable coupler. Phys Rev A 2013;87:043837.
[14] Arnold VI. Mathematical methods of classical mechanics. New York: Springer-Verlag; 1997.
[15] Lederer F, Stegeman GI, Christodoulides DN, Assanto G, Segev M, Silberberg Y. Discrete solitons in optics. Phys Rep 2008;463:1.
[16] Szameit A, Blömer D, Burghoff J, Schreiber T, Pertsch T, Nolte S, Tünnermann A, Lederer F. Discrete nonlinear localization in femtosecond laser written waveguides in fused silica. Opt Exp 2005;13:10552.
[17] Vicencio RA, Johansson M. Discrete soliton mobility in two-dimensional waveguide arrays with saturable nonlinearity. Phys Rev E 2006;73:046602.
[18] Naether U, Vicencio RA, Johansson M. Peierls-nabarro energy surfaces and directional mobility of discrete solitons in two-dimensional saturable nonlinear schrödinger lattices. Phys Rev E 2011;83:036601.
[19] Naether U, Vicencio RA, Stepić M. Mobility of high-power solitons in saturable nonlinear photonic lattices. Opt Lett 2011;36:1467.
[20] Kidd RA, Olsen MK, Corney JF. Quantum chaos in a bose-hubbard dimer with modulated tunneling. Phys Rev A 2019;100:013625.
[21] Mondal S, Greschner S, Mishra T. Phys Rev A 2019;100:013627.
[22] Wiggins S. Introduction to applied nonlinear dynamical systems. New York: Springer; 2003.
[23] Naether U, Martínez AJ, Guzmán-Silva D, Molina MI, Vicencio RA. Self-trapping transition in nonlinear cubic lattices. Phys Rev E 2013;87:0162914.
[24] Bustamante CA, Molina MI. Universal features of self-trapping in nonlinear tight-binding lattices. Phys Rev B 2000;62:15287.
[25] Albiez M, Gati R, Fölling J, Hunsmann S, Cristiani M, Oberthaler MK. Direct observation of tunneling and nonlinear self-trapping in a single bosonic josephson junction. Phys Rev Lett 2005;95:010402.
[26] Ekert AK. Quantum cryptography based on bell's theorem. Phys Rev Lett 1991;67:661.